ACS Catalysis

Research Article

pubs.acs.org/acscatalysis

Ring-Substituted α-Arylalanines for Probing Substituent Effects on the Isomerization Reaction Catalyzed by an Aminomutase

Nishanka Dilini Ratnayake,[†,∥] Nan Liu,[†,§,∥] Leslie A. Kuhn,*[,§,‡] and Kevin D. Walker*[,‡,†]

[†]Department of Chemistry, [‡]Department of Biochemistry and Molecular Biology, and [§]Computer Science & Engineering, Michigan State University, East Lansing, Michigan 48824, United States

Supporting Information

ABSTRACT: β-Amino acids are emerging as an important class of compounds in medicinal chemistry. β-Aryl-β-alanines show antiepileptogenesis activity, while others have been used to synthesize antibiotic β-peptides. To assess the utility of a methylidene imidazolone-dependent *Pantoea agglomerans* phenylalanine aminomutase (*Pa*PAM) for making non-natural β-amino acids, we surveyed the substrate specificity of *Pa*PAM with several commercially available (*S*)-arylalanine substrates. Here, we report the Michaelis−Menten parameters and catalytic efficiency of *Pa*PAM for each substrate. Compared to phenylalanine, substrates containing substituents that were either electron-withdrawing or -donating through resonance or inductive effects affected the k_{cat} of *Pa*PAM. Generally, the turnover and catalytic efficiency of *Pa*PAM for the *meta*-isomers were better than for the corresponding *para*- and *ortho*-isomers, with some exceptions. *Pa*PAM principally synthesizes the β-amino acids at >90% and the cinnamate byproducts at <10% for 11 of the 19 productive substrates. The yield from other substrates was 14−65% of the cinnamate analogue. Further, to explain the determinants of substrate selectivity of *Pa*PAM, a series of substrates with substituents on the aryl ring were docked into the crystal structure of the active site. Induced fit of the protein to accommodate different substituents was modeled computationally by SLIDE docking and Szybki energy minimization. The results provide insights into the roles of substrate orientation and conformational flexibility in turnover and indicate which terms of the interaction energy account for the experimentally observed K_M values, which largely determine catalytic efficiency. Substrate selectivity of *Pa*PAM is significantly influenced by steric barriers created by specific active-site residue interactions with the substituted aryl portion of the substrate.

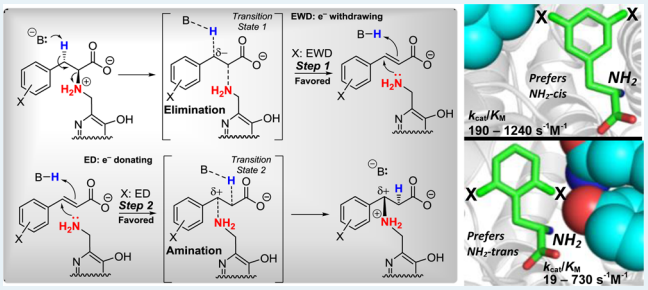

KEYWORDS: *mechanism, MIO, Hammett correlation, kinetics, computational modeling, substrate specificity*

INTRODUCTION

β-Amino acids are gaining use as building blocks for synthetic β-peptide oligomers that are used as biologically active antibiotics.[1] These β-peptides form ordered secondary structures similar to α-peptides yet are less prone to cleavage than their α-peptide counterparts by most peptidases *in vivo*. In addition, biosynthesizing novel (*S*)-β-amino arylalanines, such as *o*-methyl-β-phenylalanine, has potential application in the synthesis of a pyrazole heterocycle compound that inhibits the function of a lysosomal serine protease cathepsin A (CatA). This inhibition of CatA was shown to prevent the development of salt-induced hypertension.[2] *m*-Fluoro-β-phenylalanine has also been used as an intermediate in the synthesis of a potent chemokine receptor CCR5 antagonist.[3]

Enzymatic resolution and catalysis are described as elegant approaches to access enantiopure β-amino acids. Phenylalanine aminomutases from the bacterium *Pantoea agglomerans* (*Pa*PAM, EC 5.4.3.11) and an isozyme from *Taxus* plants (*Tc*PAM, EC 5.4.3.10) use a 4-methylidene-1*H*-imidazol-5(4*H*)-one (MIO) prosthetic group to isomerize (2*S*)-α-phenylalanine to β-phenylalanine. *Tc*PAM makes the (3*R*)-β-amino acid, a precursor of the phenylisoserine side chain on the pathway to the antimitotic compound paclitaxel.[4] In an earlier study, *Tc*PAM was shown to convert several variously modified α-arylalanines to their cognate β-isomers.[5] In contrast, *Pa*PAM makes the (3*S*)-β-phenylalanine antipode on the biosynthetic pathway to the antibiotic andrimid (Figure 1).[6] Knowing the substrate scope of *Pa*PAM could increase the range of novel enantiopure β-arylalanines obtained biocatalytically.

Both PAMs belong to a class I lyase-like superfamily of catalysts,[6−9] along with other MIO-dependent aminomutases. A phenylalanine aminomutase from *Streptomyces maritimus* (*Sm*PAM) described earlier as a lyase at physiological conditions was recently characterized as an aminomutase at lower temperatures.[7] Tyrosine aminomutases (*Cc*TAM and *Sg*TAM) are used on the biosynthetic pathways to the cytotoxic chondramides in *Chondromyces crocatus*[10] and to the enediyne antitumor antibiotic C-1027, of the neocarzinostatin family, made by *Streptomyces globisporus*.[11] A recently characterized aminomutase biosynthesizes (*R*)-2-aza-β-tyrosine from 2-aza-α-

Received: April 9, 2014
Revised: July 23, 2014
Published: July 29, 2014

   dx.doi.org/10.1021/cs500474s | ACS Catal. 2014, 4, 3077−3090

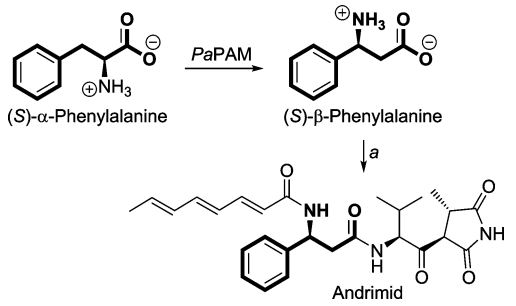

Figure 1. Partial andrimid biosynthetic pathway starting from (*S*)-*β*-phenylalanine via (*S*)-*α*-phenylalanine. (a) Several steps.

tyrosine found on the biosynthetic pathway to the enediyne kedarcidin in *Streptoalloteichus*.[12]

Recent structural characterization of *Pa*PAM supports the formation of an NH_2-MIO adduct, where the amino group of the substrate is covalently attached to the enzyme during *α*/*β*-isomerization (Figure 2).[13] A proton and the NH_2-MIO group

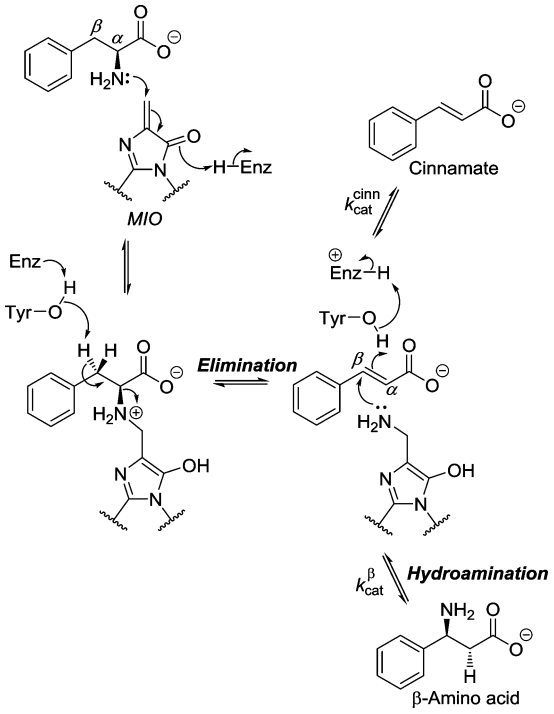

Figure 2. Mechanism of the MIO-dependent isomerization catalyzed by *Pa*PAM. MIO, 4-methylidene-1*H*-imidazol-5(4*H*)-one; k_{cat}^{cinn}, the rate at which the cinnamate byproduct is released; k_{cat}^{β}, the rate at which the *β*-amino acid product is released.

are eliminated from the substrate to form a cinnamate intermediate (released occasionally as a minor byproduct), followed by hydroamination of the intermediate from NH_2-MIO to form the *β*-amino acid.

The broad substrate specificity of *Tc*PAM encouraged us to investigate, herein, the substrate specificity of the related MIO phenylalanine aminomutase. In addition, structural and mechanistic studies on MIO-based aminomutases are increasing our understanding of the reaction chemistry of the enzymes in this family.[9,13,15−19] Here, to gain further insights on these enzymes, we used computational chemistry to analyze how structural interaction energies relate to the *Pa*PAM isomerization kinetics of substrates with different aryl rings. We propose that *Pa*PAM reaction chemistry is influenced by different properties of the substrate, including sterics, and the magnitude and direction of electronic effects of the substituents on the aryl ring.

MATERIALS AND METHODS

Gene Expression and Purification of *Pa*PAM. Luria−Bertani medium (1 L) supplemented with kanamycin (50 *μ*g/mL) was inoculated with 5 mL of an overnight culture of *E. coli* BL21(DE3) cells engineered to express the *papam* cDNA from the pET-24b(+) vector as a C-terminal His_6-tagged *Pa*PAM. These cultures were grown at 37 °C to an optical density of $A_{600} \sim 0.6$. *Pa*PAM expression was induced with isopropyl-*β*-D-thiogalactopyranoside (100 *μ*M) at 16 °C, and the cultures were grown for 16 h. The subsequent steps were performed at 4 °C, unless indicated otherwise. Cells were harvested by centrifugation at 6,000*g* (15 min), and the cell pellet was resuspended in lysis buffer (50 mM sodium phosphate buffer containing 5% (v/v) glycerol, 300 mM NaCl, and 10 mM imidazole, pH 8.0). The cells were lysed by sonication (Misonix sonicator, Farmingdale, NY), and the lysate was centrifuged at 9,700*g* (45 min) and then at 102,000*g* (1 h) to remove cell debris and light membranes. The resultant crude, C-terminal His_6-tagged aminomutase in the soluble fraction was purified by Nickel-nitrilotriacetic acid (Ni-NTA) affinity chromatography according to the protocol described by the manufacturer (Qiagen, Valencia, CA). *Pa*PAM fractions, eluting in 250 mM imidazole, were concentrated by size-selective centrifugal filtration (Centriprep centrifugal filter units, 30,000 MWCO; Millipore); the buffer was exchanged with 50 mM sodium phosphate buffer containing 5% (v/v) glycerol (pH 8.0). The purity of the concentrated enzyme was assessed by SDS−PAGE with Coomassie blue staining, and the quantity was determined by the Bradford protein assay. The overexpressed *Pa*PAM (~59 kDa) was obtained at 95% purity (~25 mg/L).

Assessing the Substrate Specificity of *Pa*PAM for (2*S*)-*α*-Phenylalanine Analogues. (*S*)-*α*-Phenylalanine and each of its analogues (1 mM) (see Supporting Information) were incubated for 2 h with *Pa*PAM (50 *μ*g) in 1 mL assays of 50 mM phosphate buffer (pH 8.0) containing 5% glycerol. Control assays contained all ingredients except that either the substrate or enzyme was omitted. Each reaction was quenched by acidifying to pH 2−3 (6 M HCl). Three internal standards (*m*-fluoro-*β*-phenylalanine, *p*-methyl-*β*-phenylalanine, and *β*-phenylalanine at 20 *μ*M) were used, respectively, to quantify three sets of biosynthetic *β*-amino acids products: set 1, *β*-phenylalanine; *o*-, *m*-, and *p*-methyl-; *o*-, *m*-, and *p*-methoxy-; *m*- and *p*-nitro-; *m*- and *p*-chloro-*β*-phenylalanine; and (2-furyl)-*β*-alanine; set 2, *o*- and *p*-fluoro; *m*- and *p*-bromo-*β*-phenylalanine; and (2-thienyl)- and (3-thienyl)-*β*-alanine; and set 3, *m*-fluoro-*β*-phenylalanine (see Supporting Information for *β*-amino acid resources). Two internal standards (*p*-methylcinnamic acid and cinnamic acid at 20 *μ*M) were used, respectively, to quantify two sets of biosynthetic aryl acrylic acid products: set 1, cinnamic acid, *o*-, *m*-, and *p*-fluorocinnamic acid, and (2-thienyl)- and (3-thienyl)-acrylic acid; set 2, *o*-, *m*-, and *p*-methyl-; *o*-, *m*-, and *p*-methoxy-; *m*- and *p*-nitro-; *m*- and *p*-chloro-; *m*- and *p*-bromo-cinnamic acid; and (2-furyl)-acrylic acid (see Supporting Information). After acidifying the reactions, the aryl acrylates were extracted with diethyl ether (2 × 2 mL). The remaining aqueous fractions were basified to pH 10 (6 M NaOH) and treated with ethylchloroformate (50 *μ*L) for 10 min. Each reaction was basified again to pH 10, a

dx.doi.org/10.1021/cs500474s | ACS Catal. 2014, 4, 3077−3090

second batch of ethylchloroformate (50 μL) was added, and each was stirred for 10 min. The solutions were acidified to pH 2−3 (6 M HCl) and extracted with diethyl ether (2 × 2 mL). For each sample, the diethyl ether fractions were separately combined. The organic fraction was removed under vacuum, and the resulting residue was dissolved in ethyl acetate/methanol (3:1, v/v) (200 μL). The solution was treated with excess (trimethylsilyl)diazomethane until the yellow color persisted. The derivatized aromatic amino acids and aryl acrylates were quantified by GC/EI-MS (see Supporting Information). The peak area was converted to concentration by solving the linear equation obtained from the standard curves constructed with the corresponding authentic standards, quantified by GC/EI-MS (Figures S1−S19 of the Supporting Information).

Kinetic Parameters of *Pa*PAM for (2*S*)-α-Phenylalanine Analogues. *Pa*PAM (10, 25, 50, or 100 μg/mL) was incubated with each productive substrate (1000, 2000, or 2250 μM) in 12 mL assays to establish linearity with respect to time at a fixed protein concentration at 31 °C. Aliquots (1 mL) were withdrawn from each assay at 0.5 h intervals over 5 h, and the reactions were quenched by adding 6 M HCl (100 μL). The products were derivatized and quantified as described above, and steady state conditions for each substrate were determined. To calculate the kinetic constants, each substrate was varied (10−2250 μM) in separate assays under the predetermined steady state conditions. The resultant β-arylalanine and aryl acrylate products were quantified after terminating the reaction as described previously. Kinetic parameters (K_M and k_{cat}^{total}) were determined from Hanes−Woolf plots by plotting [S]/*v* against [S] (R^2 = 0.97−0.99) (Figures 20S−38S of the Supporting Information), where k_{cat}^{total} = (k_{cat}^{β} + k_{cat}^{cinn}); the sum of the production rates of the β-arylalanine and aryl acrylate, respectively. The latter rates were determined from Hanes−Woolf plots.

Inhibition Assays for Nonproductive Substrates. (2*S*)-α-Phenylalanine (at 10, 20, 40, 80, 100, 200, 300, 500, 750, and 1000 μM) and *Pa*PAM (10 μg, 0.17 nmol) were mixed and incubated separately for 40 min with nonproductive substrates *o*-chloro-, *o*-bromo-, or *o*-nitro-(*S*)-α-phenylalanine (at 50, 100, and 200 μM). The products were derivatized and quantified as described earlier. Inhibition constants (K_I) were calculated by nonlinear regression analysis using GraphPad Prism 6 Software (La Jolla, CA).

Modeling Substrate-*Pa*PAM Structural Interactions to Understand Selectivity. To understand the differences in catalytic efficiency, which are largely dictated by differences in K_M, the substrates were modeled in the *Pa*PAM active site. Active configurations of the substrates were generated by overlaying their aryl rings onto the active conformation of α-phenylalanine in the crystal structure by using molecular editing in PyMOL 1.5.0.4 (Schrödinger, Inc., New York, NY) and fixed reference coordinates in OMEGA 2.4.6 (OpenEye Scientific Software, Santa Fe, NM; http://www.eyesopen.com).[14,15] Since the substrates form covalent bonds with binding site residues of *Pa*PAM, their orientation is highly restricted.

The position of the *ortho*- or *meta*-substituent breaks the C2 axis of symmetry in the phenyl ring of the substrates. Thus, the ring can adopt two configurations that are consistent with the orientation of α-phenylalanine in the crystal structure. In one configuration, called the "NH_2-*cis*," the substituent on the aryl ring is on the same side as the NH_2 group of the chiral phenylalanine substrate. In the other configuration, the "NH_2-*trans*," obtained by a 180° rotation about the C_β-C_{ipso} bond, the substituent is oriented on the side opposite the NH_2 group. For energy calculations, AM1BCC charges were assigned to the substrates using molcharge 1.3.1 (Open Eye Scientific Software).[16]

Calculating Substrate-*Pa*PAM Interaction Energies. The sum of protein−ligand interaction energy [$E_{(p\text{-}l)}$] and ligand internal energy [$E_{(l)}$] values for the 22 substrates was calculated using Szybki[17−19] 1.7.0 (OpenEye Scientific Software). The electrostatic Coulombic [$E_{C(p\text{-}l)}$] and steric van der Waals (vdW) interaction energy [$E_{V(p\text{-}l)}$] terms were extracted from the $E_{(p\text{-}l)}$ term for each conformer. Steric collisions between the substrates and the binding site residues were visualized pairwise by using a PyMOL script (created by Thomas Holder of Schrödinger, Inc.) called show_bumps.py to show vdW radius overlaps of 0.1 Å or more. The residues were then grouped according to which overlaps impacted the *o*-, *m*-, and *p*- positions of substrates. The component energy terms [$E_{(p\text{-}l)}$], [$E_{C(p\text{-}l)}$], [$E_{V(p\text{-}l)}$], and [$E_{(l)}$] were calculated with two protocols to evaluate which approach led to interaction energies that best correlated with the K_M values. First, a single-point energy calculation protocol employing a Poisson−Boltzmann electrostatics model was used when the substrate was placed in the NH_2-*cis* or NH_2-*trans* configuration. The NH_2-*cis* and NH_2-*trans* conformers were evaluated without energy minimization. The binding site of the protein was kept in its crystallographic conformation to test the hypothesis that the active complex of the protein and substrate matches the crystallographic conformation observed with α-phenylalanine (PDB entry 3UNV). Second, a two-step protocol recommended by OpenEye Scientific Software was used to explore whether energy minimization could improve the modeling of *Pa*PAM-substrate interactions by reducing any repulsive interactions. The backbone residues of *Pa*PAM were fixed, with the substrates in either the NH_2-*cis* or NH_2-*trans* configuration. Protein side chains within 4 Å of the substrates were then allowed to move toward an energy minimum, using the exact Coulomb electrostatics model. Because vdW clashes lead to large, unfavorable interaction energies, this energy minimization protocol reduces vdW overlap by small shifts in active site residues when possible. The energy estimate of each minimized configuration was then refined using the above single-point energy calculation with the Poisson−Boltzmann electrostatics model.

As an alternative approach, SLIDE (version 3.4) docking[20,21] was used to model potential conformational changes of the protein and substrate upon binding. SLIDE rotated active site residues to remove or reduce vdW overlap, while the phenylalanine ligands were fixed to maintain their initial NH_2-*cis* or NH_2-*trans* configuration.

To identify any additional steric or electrostatic factors important for the activity of *Pa*PAM substrates, structure−activity landscape index (SALI) analysis was used to identify "activity cliffs". These cliffs represent large changes in *Pa*PAM binding affinity among structurally similar substrates.[22] For identifying activity cliffs, pairwise comparisons between substrates, structural similarity scores were performed using ROCS 2.4.2 software (OpenEye Scientific Software).[23] The SALI score was measured as $SALI_{(i,j)} = |(K_{Mi} - K_{Mj})|/(2 - sim(i,j))$, in which the $sim(i,j)$ value (structural similarity between molecules *i* and *j*) was measured by the ROCS Tanimoto Combo score (with a maximum value of 2, reflecting equal contributions from shape and electrostatic match terms),

dx.doi.org/10.1021/cs500474s | ACS Catal. 2014, 4, 3077−3090

and K_{Mi} and K_{Mj} were the experimental K_M values of molecules i and j.

RESULTS AND DISCUSSION

Overview of the PaPAM Mechanism. The *Pa*PAM reaction goes through a cinnamate intermediate after elimination of the amino group and benzylic hydrogen from the α-amino acid substrate. Earlier deuterium isotope studies ($k_H/k_D > 2$) on a related aminomutase *Tc*PAM suggest the deprotonation step of the elimination reaction is rate-determining.[24] The coupling between the amine group of the substrate and the MIO is proposed to make a good alkyl ammonium leaving group. α,β-Elimination of the β-hydrogen and α-alkyl ammonium can advance through different routes. The concerted, one-step E2 (bimolecular elimination) mechanism proceeds through base-catalyzed removal of an acidic proton and a leaving group. By comparison, the two-step E1cB (unimolecular conjugate-base elimination) uses base-catalysis to remove a proton vicinal to a poor leaving group, yielding a carbanion intermediate. MIO-dependent aminomutase reactions likely follow an E2 or E1cB mechanism, where both depend on the rate of deprotonation of C_β, as proposed in an earlier work.[25] Thus, electron-withdrawing substituents on the aryl ring of the substrate that stabilize a δ^- charge on C_β should therefore increase the rate of the elimination step. In contrast, the two-step E1 (unimolecular elimination) reaction is not likely for MIO-dependent reactions. The attached, electron-withdrawing carboxylate of the substrate would destabilize the C_α-carbocation formed after displacement of the NH_2-MIO adduct (Figure 3A).

The final reaction sequence of the MIO-dependent aminomutases involves an α,β-addition reaction, where the NH_2-MIO and a proton (H^+) add across the double bond of the acrylate intermediate. To obtain the β-amino acid in a concerted hydroamination, the polarity of the C_β (δ^+) needs to be opposite of that in the earlier elimination sequence. Here, the nucleophilic NH_2-MIO binds to C_β, and the electrophilic H^+ attaches to C_α (Figure 3B).

Alternatively, *Pa*PAM could use a stepwise addition sequence where the nucleophile (NH_2-MIO) couples to form a 1,4-Michael adduct. This conjugate addition route benefits from an electropositive (δ^+) C_β by delocalizing the π-electrons toward the carboxylate of the substrate. Theoretically, a substituent that places negative charge inductively within the ring or mesomerically on C_{ipso} of the β-aryl acrylate intermediate should also strengthen the formation of a δ^+ on C_β. These types of electrostatic considerations, along with binding affinity, were considered to explain the hydroamination reaction of *Tc*PAM for aryl acrylate substrates.[26,27]

In earlier accounts, the Michael addition mechanism was proposed,[28,29] but a presumed resonance structure has two repelling oxyanions on the carboxylate of the reactant that normally forms a monodentate salt bridge (Figure 4a), as evidenced in the *Pa*PAM crystal structure.[13] To alleviate buildup of this electrostatic repulsion, we propose that near-concerted protonation and amination of the π-bond likely minimizes the formation of the unfavorable dianion (Figure 4b). A contrasting pathway is envisioned to first add a proton at C_α of the acrylate intermediate. The resulting intermediate has a positive charge (δ^+) on the benzylic C_β, which is resonance stabilized by the aryl ring and further stabilized by electron-releasing substituents (Figure 4c). Rapid nucleophilic attack by the NH_2-MIO on the carbocation would ensue to complete β-amino acid catalysis.

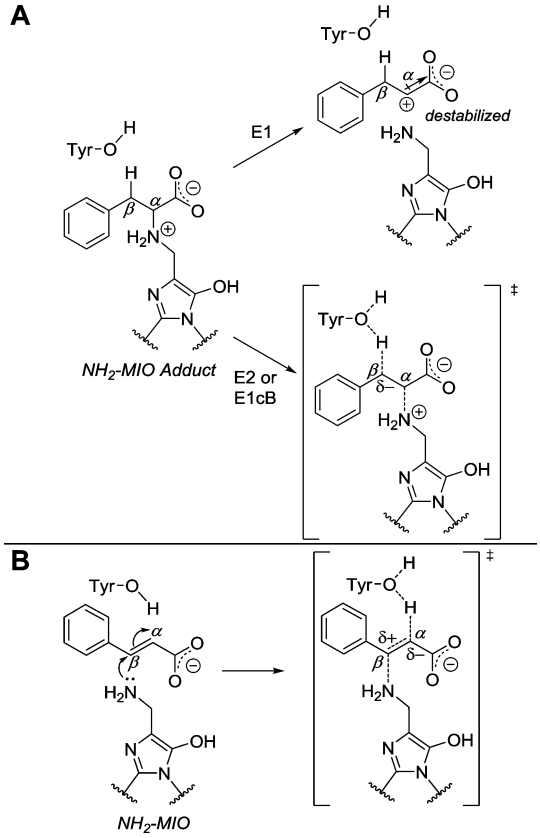

Figure 3. (A) Proposed elimination mechanisms for the displacement of the NH_2-MIO adduct. E1, unimolecular; E2, bimolecular; and E1cB, conjugate-base eliminations. (B) Concerted hydroamination of the acrylate intermediate. Shown is a transition state intermediate (right) highlighting the polarization of the π-bond in which the nucleophilic NH_2-MIO and the electrophilic H^+ approach C_β and C_α, respectively.

Electronic Effects of *ortho*-, *para*-, and *meta*-Substituents. To gain further insights into the mechanism of *Pa*PAM, the substrate specificity was queried with 19 phenylalanine analogues and 3 heteroaromatic compounds. The substituents on the phenyl ring varied in position, size, inductive and mesomeric effects, polarizability, hydrophobicity, and the ability to form H- and halogen-bonds. The kinetic parameters of *Pa*PAM for the natural substrate (**1**) are used to compare against the values for each analogue (**2**–**22**).

In general, the relative catalytic efficiency (Table 1) for each analog was negatively affected by a decrease in k_{cat}^{total} and/or increase in K_M. In addition, the linear correlation coefficient was calculated between the binding energy and experimental K_M values for different models of substrate positioning in the *Pa*PAM binding site. Each substrate was placed in the crystallographic orientation of the α-phenylalanine substrate, and the side chains of *Pa*PAM were modeled without energy minimization in positions guided by the crystal structure. This crystal structure-like model correlated better with K_M values than did flexibility modeling of substrate interactions by using SLIDE or two alternative energy minimization protocols.

Substituent Effects on Michaelis Parameters. meta-Substituents. The relative catalytic efficiencies were highest for *m*-halogenated substrates (**2**–**4**) (Table 1). The K_M values of *Pa*PAM for *m*-bromo (**2**) and *m*-chloro (**4**) substrates were

dx.doi.org/10.1021/cs500474s | ACS Catal. 2014, 4, 3077–3090

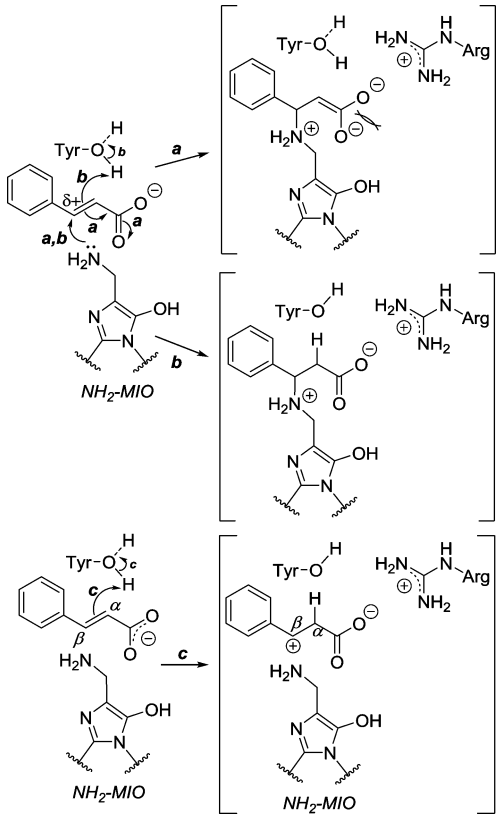

Figure 4. (Route a) A stepwise Michael-addition pathway. Shown is an intermediate adduct (top right) with the π-electrons delocalized into the carboxylate group forming a repelling dianion prior to C_α-protonation. (Route b) Concerted hydroamination of the acrylate π-bond. Shown is an intermediate (middle right) with maximal charge separation between repelling negative charges in the carboxylate group and the cation and anion. (Route c) A stepwise hydroamination sequence. Shown is a proposed intermediate (bottom right) resulting from C_α-protonation as the first step, which places a positive charge at C_β. C_β is now primed for nucleophilic attack by the NH_2-MIO adduct.

only negatively affected ~2-fold, and the k_{cat}^{total} values remained essentially unchanged compared to the parameters for **1** (Table 1). Interestingly, the relative k_{cat}^{total} for the *m*-fluoro substrate **3** was ~10-fold lower (0.031 s^{-1}) than that for **1**, **2**, and **4**, yet the 5-fold lower K_M of *Pa*PAM for **3** made the k_{cat}^{total}/K_M similar to those for **1**, **2**, and **4**. The latter suggests that **3** binds tighter than **2** and **4**, which carry halogens (Br and Cl) with larger atomic radii of 185 and 175 pm, respectively, compared to the smaller F (147 pm) of **3**. In addition, the fluoro group, through some as yet unknown process, causes **3** to bind better than the natural substrate containing a smaller H atom.

Analysis of other *meta*-substituted substrates showed the catalytic efficiencies for *m*-nitro (**9**), *m*-methoxy (**11**), and *m*-methyl (**13**) analogues were 6- to 10-fold lower than that for **1**. The *m*-nitro of **9** only reduced the relative k_{cat}^{total}/K_M of *Pa*PAM by 5.7-fold due to the modest 2.2- and 2.6-fold negative effects on k_{cat}^{total} and K_M, respectively, compared with that of **1** (Table 1). To further evaluate the mechanistic basis of the differences in turnover by *Pa*PAM for various *meta*-substituted substrates, we gauged the dependence of the relative turnover rate on the substituent of the substrate.

The Hammett plot between the calculated $\log(k_{cat}^{mX}/k_{cat}^{H})$ of *Pa*PAM and substituent constants (σ)[30] for the *meta*-substituted (*m*X) arylalanines (*m*-bromo (**2**), *m*-chloro (**4**), *m*-nitro (**9**), *m*-methoxy (**11**), and *m*-methyl (**13**)) follow a concave-down, parabolic regression curve[31] (Figure 5A). The fastest reactions at the apex of the curve occurred with the *m*-

Table 1. Kinetic Parameters[a] of *Pa*PAM for Various Substituted Aryl and Heteroaromatic Substrates

	R	K_M	k_{cat}^{β}	k_{cat}^{cinn}	k_{cat}^{total}	k_{cat}^{total}/K_M
1		168 (7)	0.301 92.8%	0.022 7.2%	0.323 (0.013)	1.93 (0.20)
2	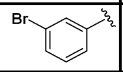	339 (15)	0.396 93.9%	0.024 6.1%	0.420 (0.014)	1.24 (0.12)
3	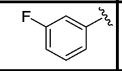	27 (5)	0.027 85.2%	0.004 14.8%	0.031 (0.002)	1.2 (0.4)
4	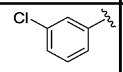	432 (26)	0.462 95.2%	0.022 4.8%	0.484 (0.02)	1.12 (0.14)
5	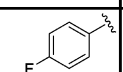	29 (1)	0.020 85.7%	0.003 14.3%	0.023 (0.001)	0.79 (0.06)
6	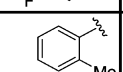	88 (6)	0.055 83.6%	0.009 16.4%	0.064 (0.002)	0.73 (0.09)
7	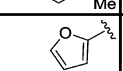	415 (79)	0.143 34.8%	0.093 65.2%	0.236 (0.01)	0.588 (0.066)
8	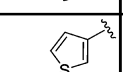	337 (27)	0.139 97.2%	0.004 2.8%	0.143 (0.004)	0.428 (0.063)
9	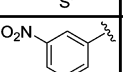	430 (15)	0.136 92.6%	0.01 7.4%	0.146 (0.003)	0.340 (0.025)
10	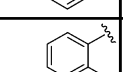	73 (6)	0.021 95.5%	0.001 4.5%	0.022 (0.001)	0.31 (0.04)
11	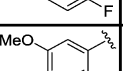	990 (124)	0.201 99.0%	0.002 1.0%	0.203 (0.012)	0.209 (0.050)
12	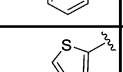	132 (5)	0.024 90.9%	0.002 9.1%	0.026 (0.001)	0.19 (0.02)
13	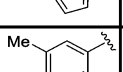	204 (4)	0.048 78.3%	0.010 21.7%	0.058 (0.001)	0.19 (0.01)
14	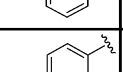	491 (82)	0.050 94.1%	0.003 5.9%	0.053 (0.003)	0.11 (0.03)
15	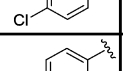	525 (44)	0.043 95.6%	0.002 4.4%	0.045 (0.001)	0.09 (0.01)
16	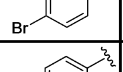	163 (9)	0.010 63.6%	0.003 36.4%	0.013 (0.001)	0.082 (0.010)
17	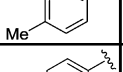	752 (39)	0.025 48.0%	0.013 52.0%	0.038 ($<10^{-3}$)	0.050 (0.005)
18	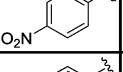	1187 (76)	0.022 97.7%	0.0005 2.3%	0.022 ($<10^{-3}$)	0.019 (0.002)
19	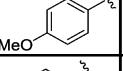	164 (7)	0.002 70.0%	0.0007 30.0%	0.003 ($<10^{-3}$)	0.02 ($<10^{-2}$)
20	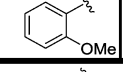					
21	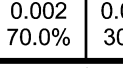					
22	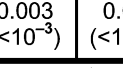					

[a]Standard errors are in parentheses. Units: s^{-1} for k_{cat}, μM for K_M, and $s^{-1} \cdot \mu M^{-1} \times 10^3$ for k_{cat}^{total}/K_M. Compounds **20**–**22**, not productive.

dx.doi.org/10.1021/cs500474s | ACS Catal. 2014, 4, 3077–3090

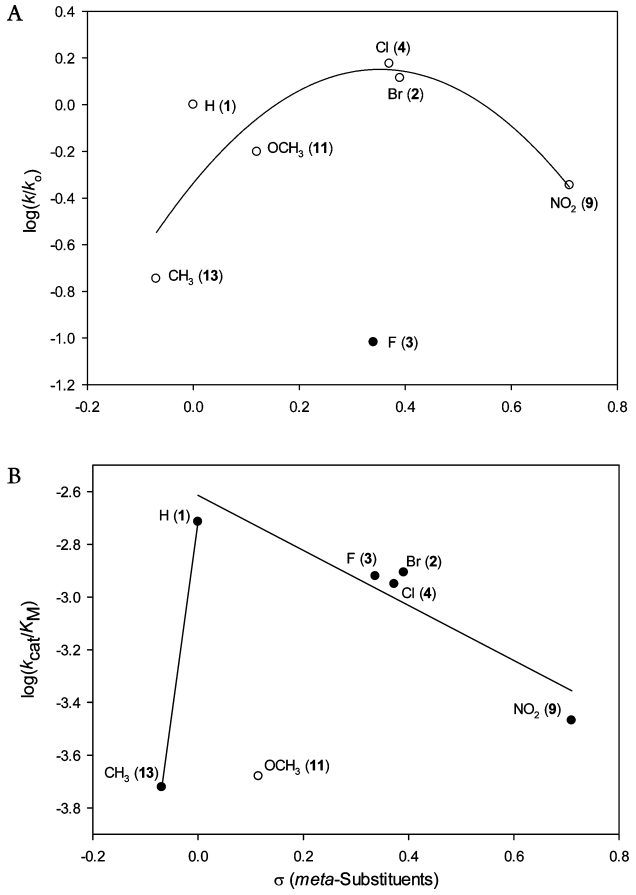

Figure 5. (A) Dependence of the observed $\log(k_{cat}^{mX}/k_{cat}^{H})$ [designated as $\log(k/k_0)$] on the Hammett substituent constant for the *Pa*PAM-catalyzed isomerization of *meta*-substituted α-arylalanines. Here, k_{cat}^{mX} is k_{cat}^{total} for entries **2**–**4**, **9**, **11**, and **13**; k_{cat}^{H} is k_{cat}^{total} for entry **1**. Correlation coefficient (R) = 0.84. The outlier *m*-fluoro substrate **3** (filled circle) appears at $\log(k/k_0) = -1.02$; $\sigma = 0.06$; $SE_{\bar{x}} \pm 0.019$–0.033. (B) Dependence of the observed $\log(k_{cat}^{mX}/K_M)$ [designated as $\log(k_{cat}/K_M)$] on the Hammett substituent constant for the *Pa*PAM-catalyzed isomerization of *meta*-substituted α-arylalanines (**1**–**4**, **9**, **11**, and **13**). Correlation coefficients: (R) = 0.93 for the linear regression of entries **1** and **13**, with a positive-slope (ρ = 14). The outlier *m*-methoxy substrate **11** (open circle) appears at $\log(k_{cat}/K_M) = 2.32$; $\sigma = 0.12$; $SE_{\bar{x}} \pm 0.024$–0.085.

bromo and *m*-chloro substrates and the slowest with *m*-methyl and *m*-nitro, at the extremes. The *m*-methoxy substituent reacted at an intermediate rate.

m-Halogens and m-Nitro. Halogens are a group of substituents of the "push–pull" type. They withdraw electron density by induction and donate electrons by resonance, depending on the type of reaction. The overall effect of the halogens is considered electron-withdrawing as estimated by their Hammett substituent constants. *m*-Bromo (**2**) and *m*-chloro (**4**) substrates, however, occupy an ambiguous position at the apex of the Hammett plot (Figure 5A). The right side of the correlation plot tends toward a slope (ρ) < 0 and suggested the rate of the *Pa*PAM reaction was slowed by electron-withdrawing substituents.

The $\log(k_{cat}^{mX}/k_{cat}^{H})$ for *m*-nitro substrate **9** fits on the negative slope ($\rho \approx -1.4$) of the correlation curve (Figure 5A). The strong electron-withdrawing *m*-nitro group is foreseen to accelerate deprotonation of C_β that produces a transient δ^- on the elimination step (Figure 6A). In turn, the nitro group

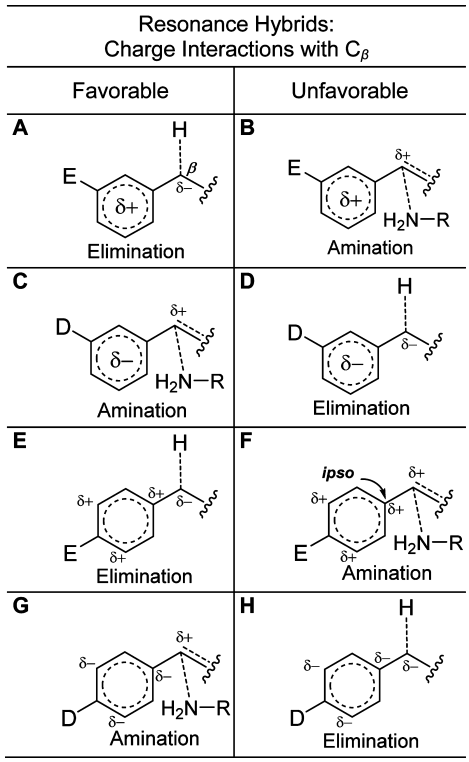

Figure 6. Resonance hybrids formed from electron-donating (D) or -withdrawing (E) substituents on the phenyl ring. An increase or decrease in electron density, caused by the substituent, within the ring or at C_{ipso} is predicted to support a transient δ^+ or δ^-, respectively, at C_β. Resonance hybrids that support an electronegative (δ^-) C_β are proposed to increase the rate of initial elimination, while those that support an electropositive (δ^+) C_β are viewed to increase the hydroamination rate.

was anticipated to affect the β-amination step, which forms a transient δ^+ on C_β (Figure 6B). The resonance hybrid of the *m*-nitro group places δ^+ on carbons flanking, but not directly on, C_{ipso}. The *m*-nitro group was therefore expected to slow the amination rate of the *Pa*PAM reaction involving **9** compared to that for **1**. The *m*-nitrocinnamate (7.4%)/*m*-nitro-β-amino acid (92.6%) product ratio apportioned similar to that of analogous products made from **1**. This result suggested that the *m*-nitro of **9** likely deterred the hydroamination of the *m*-nitrocinnamate intermediate less than imagined. Thus, the intermediate was still released as a byproduct presumably at a slower rate than the rate of hydroamination.

In contrast, substrates **2** and **4** were turned over ~3-fold faster than **9** (Table 1). The "push–pull" effect of **2** and **4** likely tells that electron-release by *m*-bromo and *m*-chloro reduces the electron-withdrawing magnitude that negatively affects the rate, as did the *m*-nitro of **9**. The balanced electron-withdrawing effect of bromo and chloro likely support the transient δ^- on C_β and increases the rate of the elimination step (Figure 6A); in concert, the electron-donating effect would improve stabilization of a transient δ^+ formed during the hydroamination across the double bond of the intermediate (Figure 6C).

It is worth noting that the proportions of *m*-halo-β-amino acids (93.9% *m*-bromo-β-amino acid and 95.2% *m*-chloro-β-amino acid) and *m*-halo-cinnamate (6.1% *m*-bromo-cinnamate and 4.8% *m*-chloro-cinnamate) made by *Pa*PAM from **2** and **4**, respectively, were similar to those of analogous products made from **1** (Table 1). Thus, the amination of the *m*-halocinnamate

dx.doi.org/10.1021/cs500474s | *ACS Catal.* 2014, 4, 3077–3090

intermediates was likely not significantly affected by the substituents. This observation supports a mechanism where release of the intermediate as a byproduct is slower than hydroamination.

Interestingly, based on Hammett constants, the inductive effects of the fluoro group (σ = 0.34) on an aryl ring are in principle similar to those of the chloro- (σ = 0.37) and bromo- (σ = 0.39) substituents.[30] Therefore, it was surprising that the *m*-fluoro substrate **3** had a significantly lower $\log(k_{cat}^{mX}/k_{cat}^{H})$ value and did not fit the Hammett correlation for the *meta*-substituent series (Figure 5A). The significant decrease (~10-fold) in k_{cat}^{cinn} and k_{cat}^{β} of *Pa*PAM for **3** (compared with the same parameters for **1**) suggested that the *m*-fluoro substituent affected the chemistry at C_β during the elimination *and* the hydroamination steps. The higher proportion of *m*-fluorocinnamate (14.8%) relative to *m*-fluoro β-amino acid (85.2%) made by *Pa*PAM from **3**, (compared with the cinnamate (7.2%) and β-amino acid (92.8%) products made from **1**) suggested that the electronic effects of the *m*-fluoro compound affected the amination step more than the elimination step.

m-Methoxy and m-Methyl Substrates. *m*-Methoxy and *m*-methyl substrates **11** and **13**, respectively, appear on the Hammett correlation plot where the slope (ρ) ≈ +2.9 (Figure 5A). This suggested that the *Pa*PAM rate was markedly slowed by stronger electron-donating *meta*-substituents. The larger 9.3-fold decrease in the relative k_{cat}^{total}/K_M for **11** was principally influenced by the 5.9-fold increase in K_M compared with that for **1**. The increased K_M suggested that the sterics of the *m*-methoxy substrate affected substrate binding. However, the k_{cat}^{total} for **11** was only 1.6-fold lower than for **1** and correlated well with the Hammett constants for *meta*-substituents (Figure 5A).

On the basis of the Hammett constant (+0.12),[30] *m*-methoxy has an electron-withdrawing component that slightly reduces the significant *meta*-substituent effect of its electron-donation into the ring by resonance. The *m*-methoxy substituent likely destabilizes the δ^- on C_β upon removal of H_β (Figure 6D) and decreases the elimination rate. Reciprocally, electron-donation by the *m*-methoxy substituent would promote formation of an electrophilic (δ^+) C_β (Figure 6C) during the amination step. Here, the electronic effects of the *m*-methoxy that deterred the elimination rate were likely offset by its rate-enhancing effects on the amination step.

An earlier study showed that *Pa*PAM catalyzes the α/β-isomerization of phenylalanine entirely intramolecularly. The results of the earlier work told that the aminomutase tightly holds the cinnamate intermediate, thus preventing it from exchanging with exogenous cinnamate added at high concentration.[29] In the current study, the *Pa*PAM-catalyzed product pool from **11** contained the *m*-methoxy-β-amino acid (99.0%) and the *m*-methoxy acrylate at 1.0%. *Pa*PAM converted **1** with less selectivity (β-isomer at 92.8%; cinnamate at 7.2%). This supported that the efficiency to aminate the acrylate intermediate to make the β-isomer of **11** was most likely facilitated by the substituent.

A methyl-substituent contributes electron density through hyperconjugation (quasi-mesomeric)[32] to the attached aryl ring and exerts resonance effects, to a lesser extent, but similar to those of methoxy.[30] The $\log(k_{cat}^{mX}/k_{cat}^{H})$ for **13** with an electron-"releasing" *m*-methyl (σ = −0.07) fits on the parabolic Hammett correlation curve (Figure 5A). The steep slope in this region suggested that the rate of the *Pa*PAM reaction is strongly affected by the electron-releasing *meta*-substituent. Despite the smaller *meta*-substituent constant for methyl than for methoxy, the mesomeric *m*-methoxy releases more electron density to the ring than the methyl does through hyperconjugation. We therefore postulated that the rate enhancement of the addition step, through a favorable transition state (Figure 6C), with **13** was not as significant as with **11**. This likely accounted for the >3.5-fold faster k_{cat}^{total} for *m*-methoxy **11** than for *m*-methyl substrate **13**.

The product pool catalyzed by *Pa*PAM from **13** contained more cinnamate analogue (21.7%) compared to that made from other *m*-substituted substrates **2**, **4**, **9**, and **11** that contained between 1.0% and 7.4%. We propose that the amination of the *m*-methyl aryl acrylate is more sensitive to the effects of the substituent. *m*-Fluoro substrate **3** was converted to the cinnamate analogue (14.8%) at a similar proportion as was **13**. Compared with **1**, it is intriguing that substrates **3** and **13**, with opposing electronic and steric properties, similarly affect the k_{cat} of *Pa*PAM and the ratio of the cinnamate/β-amino acid analogues.

The K_M of *Pa*PAM for *m*-methyl substrate **13** was only slightly affected (1.2-fold) for the less sterically demanding methyl, compared to the methoxy group of **11**. However, the k_{cat}^{total} for **13** was surprisingly 5.6-fold slower than that for **1** and nearly 4-fold slower for **11**. To help explain these observations, we look at the lone pair geometry predicted by earlier *ab initio* calculations of an isolated alcohol molecule.[33] This earlier work predicted the angle between geminal electron pairs of the oxygen atom was greater than the typical 109.5° between sp^3-hybrid orbitals. Using this principle, the methoxy group of **11** can likely place the less steric lone pairs of electrons and methyl group on the central oxygen atom in a favorable conformation so the substrate remains catalytically competent. By contrast, the methyl substituent of **13** has three overlapping sp^3-s orbitals forming the C−H bonds. Even though the methyl group of **13** is sterically smaller than the methoxy group of **11**, the tetrahedral geometry of the methyl hydrogens may cause **13** to adopt a potentially undesirable orientation for catalysis. These considerations for the *m*-methyl and *m*-methoxy groups are further supported by findings from the computational analyses, described later herein.

meta-Substituent Effects on Catalytic Efficiency. The plot between $\log(k_{cat}^{mX}/K_M)$ and σ for the *meta*-substituted (*m*X) arylalanines (Figure 5B) showed that the substituent effects on the catalytic efficiency (k_{cat}^{mX}/K_M) largely paralleled the nonlinear relationship between $\log(k_{cat}^{mX}/k_{cat}^{H})$ and σ (Figure 5A). Thus, the substituent effects on the k_{cat} value of the catalytic efficiency were not masked by the K_M. Interestingly, the *m*-fluoro (**3**) substrate fit the linear regression of the plot between $\log(k_{cat}^{mX}/K_M)$ and σ (ρ = −1.05). The effects of the electron-withdrawing *m*-fluoro substituent on the catalytic efficiency correlated well with those of *m*-chloro and *m*-bromo (Figure 5B). Substrate (**3**) was an outlier, however, on the parabolic regression plot of $\log(k_{cat}^{mX}/k_{cat}^{H})$ and σ (Figure 5A). Reciprocally, the *m*-methoxy (**11**) substrate fit the parabolic regression of the plot between $\log(k_{cat}^{mX}/k_{cat}^{H})$ and σ (Figure 5A), and was an outlier on the $\log(k_{cat}^{mX}/K_M)$ correlation plot (Figure 5B). This result suggested that the catalytic efficiency of *Pa*PAM for substrates **3** and **11** was influenced more by their affinity for *Pa*PAM than by electronic substituent effects. The relatively low K_M (27 μM) for **3** likely revealed that the acrylate intermediate and β-amino acid products were also released poorly and affected the turnover. In contrast, the high K_M (990 μM) for **11** suggested poor substrate binding, which masked the correlation between

dx.doi.org/10.1021/cs500474s | ACS Catal. 2014, 4, 3077−3090

the substituent constant of the *m*-methoxy group and catalytic efficiency.

para-Substituents. Each substrate containing a *para*-substituent (**5**, **14**–**18**) reduced the k_{cat}^{total} of *Pa*PAM by 6–25-fold compared to the value for **1** (k_{cat}^{total} = 0.323 s^{-1}). As seen for the trend with the *meta*-substituent series, the *p*-bromo and *p*-chloro substituents were turned over the fastest; the chloro substrate was turned over slightly faster. The substrates turned over the slowest by *Pa*PAM in this series contained a *p*-nitro, *p*-methyl, or *p*-methoxy (Table 1). The calculated $\log(k_{cat}^{mX}/k_{cat}^{H})$ of *Pa*PAM and substituent constants (σ) for the *para*-substituted arylalanines (*p*-fluoro (**5**), *p*-chloro (**14**), *p*-bromo (**15**), *p*-methyl (**16**), *p*-nitro (**17**), and *p*-methoxy (**18**)) do not follow a single Hammett plot (Figure 7A). By analogy, the parabolic concave-down Hammett plot for the *meta*-substituted substrates showed a gradual change in the reaction step on the *Pa*PAM pathway that was sensitive to the *meta*-substituent. Likewise, for the *para*-substituents, the intersecting linear regressions of the opposite slope (ρ) (Figure 7A) suggest the substituent effects transition from affecting the elimination step to affecting the amination step.[31]

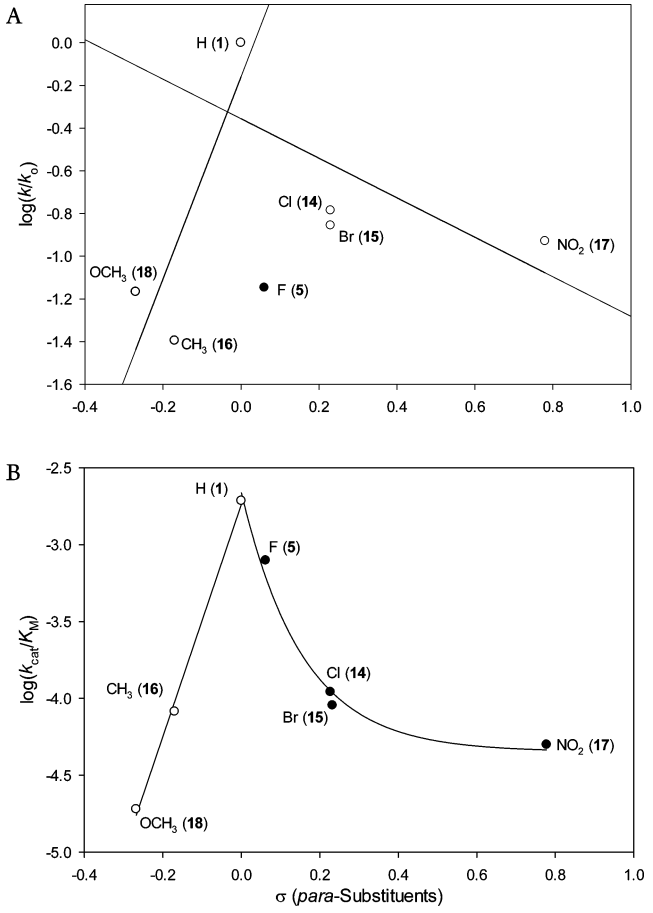

Figure 7. (A) Dependence of the observed $\log(k_{cat}^{pX}/k_{cat}^{H})$ [designated as $\log(k/k_0)$] on the Hammett substituent constant for the *Pa*PAM-catalyzed isomerization of *para*-substituted α-arylalanines. Here, k_{cat}^{pX} is k_{cat}^{total} for entries **14**, **15**, **16**, **17**, and **18**; k_{cat}^{H} is k_{cat}^{total} for entry **1**. The outlier *p*-fluoro substrate **5** (filled circle) appears at $\log(k/k_0 = -1.15$; σ = 0.06). Correlation coefficients: (R) = 0.87 for the positive-slope and (ρ = +4.74) for the linear regression of entries **1**, **16**, and **18**; (R) = 0.71 for the negative-slope and (ρ = −0.93) for the linear regression of entries **1**, **14**, **15**, and **17**; $SE_{\bar{x}}$ ± 0.018–0.038. (B) Dependence of the observed $\log(k_{cat}^{pX}/K_M)$ [designated as $\log(k_{cat}/K_M)$] on the Hammett substituent constant for the *Pa*PAM-catalyzed isomerization of *para*-substituted α-arylalanines. Here, k_{cat} is k_{cat}^{total} for entries **5**, **14**, **15**, **16**, **17**, and **18**. Correlation coefficients: (R) = 0.99 for the decay curve for entries **1**, **5**, **14**, **15**, and **17**; (R) = 1.0 for the linear regression of entries **1**, **16**, and **18** with a positive-slope (ρ = 7.50); $SE_{\bar{x}}$ ± 0.024–0.076.

The resonance hybrid of the *p*-nitro substrate **17** has a δ^+ directly on C_{ipso} attached to C_β (Figure 6E). While this was imagined to strongly increase the elimination rate (i.e., facilitates H_β proton removal), the 8.5-fold slower k_{cat}^{total} of *Pa*PAM for **17** (0.031 s^{-1}) than that for **1** (Table 1) likely resulted because the *p*-nitro slowed the hydroamination rate (i.e., deterred nucleophilic attack at C_β) (Figure 6F) more than it improved the elimination rate. The higher ratio of *p*-nitrocinnamate (52%) compared to cinnamate (7.2%) made from **1** further supports an affected hydroamination step.

Based on proximity, the effects of the electron-withdrawing *p*-chloro and *p*-bromo of substrates **14** and **15** on C_{ipso} are lower than those for the corresponding *meta*-isomers. The lone-pair electrons of the former, however, can delocalize by resonance and place a δ^- directly on C_{ipso} attached to C_β in the resonance hybrid. The δ^- will promote the amination step (Figure 6G), yet dramatically retard the deprotonation of the elimination step of the *Pa*PAM reaction (Figure 6H). Likewise, the electron-releasing *p*-methyl of **16** and *p*-methoxy of **18** also place a δ^- on C_{ipso} of the substrate via hyperconjugation and resonance, respectively. Each theoretically causes the pK_a of H_β to increase and discourages the deprotonation of the presumed rate-limiting elimination step. The Hammett substituent constants predicted the electron-releasing *p*-methyl would affect *Pa*PAM turnover (k_{cat}^{total} = 0.013 s^{-1}) more than the methoxy group, as observed (Figure 7A and Table 1). *Pa*PAM has a ρ value (+4.74) much greater than unity for the electron-donating substrates **16** and **18**, suggesting that catalysis is very dependent on the nature of these substituents. By comparison, the $\rho \approx -1.0$ for substrates **14**, **15**, and **17** suggests a moderate yet significant dependence on the electron-withdrawing strength of the substituent (Figure 7A).

In addition, the binding affinity of *Pa*PAM for **16** (K_M = 163 μM) and the natural substrate **1** (K_M = 168 μM) was similar, while the k_{cat}^{total} for **16** was 25-times slower than for **1**, further suggesting a strong sensitivity of the reaction rate to the *p*-methyl group (Table 1). Taken together, these results suggest that the magnitude and direction of the electron-releasing or -withdrawing effect of the *para*-substituents affect the isomerization rate. That is, electron-releasing substituents affect the deprotonation step of the elimination reaction, while the electron-withdrawing groups affect the nucleophilic addition step catalyzed by *Pa*PAM.

The *p*-fluoro substrate **5** was turned over by *Pa*PAM at about the same rate as the *m*-fluoro substrate **3**, but coincidentally at the same rate as the other *para*-substituted substrates. It seems that regardless of regiochemistry, the overarching electronic effect(s) of the fluoro substituent stalls the elimination and hydroamination steps. In addition, based on the β-amino acid/aryl acrylate (85.7:14.3) distribution catalyzed by *Pa*PAM from **5**, it seems that the fluoro group affects the efficiency of the β-amination step compared to the reaction involving **1**. A similar product distribution was seen herein for the *m*-fluoro substrate **3**.

para-Substituent Effects on Catalytic Efficiency. The relationship between $\log(k_{cat}^{pX}/K_M)$ and σ for the *para*-substituted (*p*X) arylalanines (Figure 7B) showed a similar

dx.doi.org/10.1021/cs500474s | ACS Catal. 2014, 4, 3077–3090

trend in substituent effects on the catalytic efficiency (k_{cat}^{pX}/K_M) as seen between $\log(k_{cat}^{pX}/k_{cat}^{H})$ for *Pa*PAM and Hammett substituent constants (Figure 7A). There was a strong, nonlinear correlation between decreasing catalytic efficiency and strongly electron-withdrawing and -donating substituents. As with the *meta*-substituents, the catalytic efficiency of *Pa*PAM was also sensitive to the *para*-substituents. Intriguingly, the dependency of the catalytic efficiency on the *para*-substituent reduced as a combination of electron-withdrawing or -donating strength and increasing K_M for the substrate (Figure 7B and Table 1). This informed us that a reduction in catalytic efficiency was principally dictated by large K_M values and not by the electronic effects of the *para*-substituent that separately affected k_{cat} (Figure 7A).

ortho-Substituents. Interestingly, the K_M values of *Pa*PAM for each of the three productive *ortho*-substrates (**6**, **10**, and **19**) varied only between 1- and 2-fold compared to that of **1**. Seemingly, the *ortho*-substituents, regardless of size, including the bulkier *o*-methoxy of **19**, did not affect substrate binding. Of the three, *Pa*PAM turned over the *o*-methyl substrate (**6**) faster (0.064 s^{-1}) than the *o*-fluoro (**10**, 0.022 s^{-1}) and *o*-methoxy (**19**, 0.003 s^{-1}) compounds (Table 1). However, each was isomerized substantially slower (5-, 14-, and 108-fold, respectively) than **1**. Similar to the *para*-substituents, *ortho*-substituents exert strong resonance and moderate inductive electronic effects that influence the chemistry at certain carbons of an aryl ring (see Figure 6). We propose that electron-donating *ortho*-substituents (methyl and methoxy) placed δ^- on C_{ipso} of the substrates. The relatively satisfactory binding (i.e., low K_M values) yet poor turnover for **6**, **10**, and **19** suggests either that *Pa*PAM binds these substrates in a catalytically ineffective orientation or that their electron-donor substituents slow the deprotonation step of catalysis. It should be noted that the *ortho*-substituents on the arylalanine substrates are positioned vicinally to the alanine side chain. The proximity of these groups to the alanyl side chain of the substrates likely creates a steric barrier that skews the aryl ring plane. A canted aryl ring would relax the sterics yet reduce potentially beneficial resonance effects of the substituents on C_β in a charged transition state that could influence substrate turnover.

We expected the *o*-bromo, *o*-chloro, and *o*-nitro substrates **20**–**22** to have productive kinetics similar to those of the corresponding *para*-isomers since *ortho*/*para*-substituents of the same type exert similar electronic effects (Figure 6E and F). Interestingly, **20**–**22** did not yield any detectable product in the enzyme reaction. However, their competitive inhibition constants (K_I) of 15.9 (±1.67), 17.7 (±2.11), and 16.9 (±3.35) μM indicate that they bind well to *Pa*PAM. The lack of turnover of **20**–**22** by *Pa*PAM was therefore likely caused by poor access of the substrates to a catalytically competent conformation.

Heteroaromatic Substrates. After understanding the *ortho*-, *para*-, and *meta*-directing character of the substituents, the influence of heteroatoms on the distribution of electron density in resonance structures of the aromatic ring was not difficult to predict. Evaluation of a resonance hybrid of 3-thienylalanine (**8**) showed that a δ^- charge resides on C_{ipso} of the thienyl ring (Figure 8A, resonance path a). We noted an analogous δ^- charge on C_{ipso} of productive substrates (**5**, **14**–**18**) containing an electron-donating *para*-substituent on the phenyl ring (see Figure 6G or H). We proposed that this electronic effect slowed the deprotonation of the presumed rate-limiting elimination step. For substrate **8**, however, the vicinal δ^-

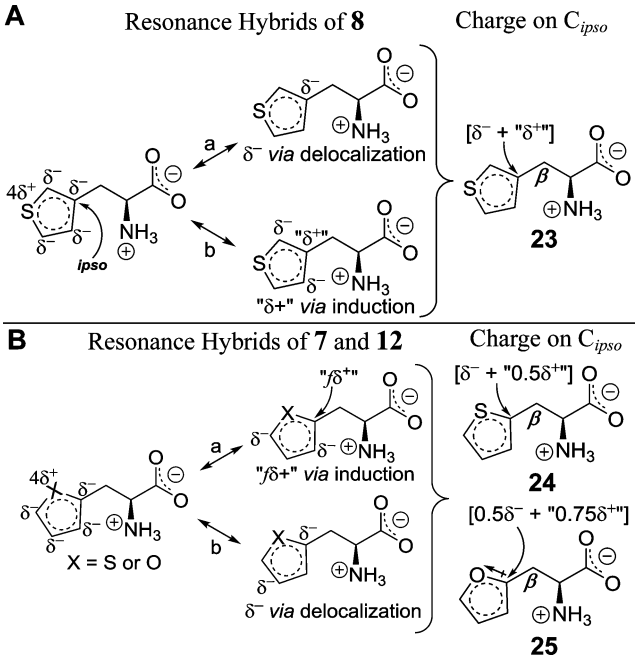

Figure 8. (A) Resonance hybrids of 3-thienylalanine (**8**) and (B) composite resonance hybrids of 2-furylalanine (**7**) and 2-thienylalanine (**12**); a dipole moment is illustrated. Also shown are the partial (δ) charges resulting from a combination of the charges present in the canonical structures obtained through delocalization of electrons in the extended aromatic π-system. The induced charges on C_{ipso} are designated in quotation marks. Charges are weighted arbitrarily by fractional numbers (f) to illustrate their relative contribution at C_{ipso} in **23**, **24**, and **25**.

charges induce a "δ^+" on the C_{ipso}, which is imagined to reduce the magnitude of the δ^- at C_{ipso} (Figure 8A, resonance path b). Thus, the lower magnitude δ^- at C_{ipso} of **8**, compared to the δ^- at C_{ipso} for **5** and **14**–**18** (0.013–0.053 s^{-1}), likely affected the rate-determining deprotonation step less, as evidenced by its 3- to 10-fold higher k_{cat}^{total} of *Pa*PAM for **8** (0.143 s^{-1}).

The effect of a reduced δ^- at C_{ipso} of **8** likely also explains why *Pa*PAM catalyzed **8** ~6-fold faster than 2-thienylalanine (**12**, 0.026 s^{-1}). One resonance hybrid of **12** has one δ^- charge vicinal to C_{ipso} (Figure 8B, resonance path a), and because of this, we assign an induced charge on C_{ipso} as "$0.5\delta^+$" to illustrate its magnitude as less than the induced "δ^+" in **8** flanked by two vicinal δ^- charges (cf. Figure 8A, route b). Another resonance hybrid of **12** has a δ^- charge on C_{ipso} (Figure 8B, resonance path b). Thus, the overall charge at C_{ipso} of **12** is represented arbitrarily as (δ^- + "$0.5\delta^+$") (Figure 8B, **24**), while that of **8** is represented as (δ^- + "δ^+") (Figure 8A, **23**). The greater δ^- charge on C_{ipso} of **12** than on **8** likely conflicts with the δ^- formed on C_β during the transition state of the deprotonation step. Thus, this effect likely slowed the *Pa*PAM reaction more when **12** was used as substrate than when **8** was used.

It was interesting that the 2-furylalanine (**7**, 0.236 s^{-1}) was turned over by *Pa*PAM ~9-fold faster than the analogous 2-thienylalanine (**12**, 0.026 s^{-1}), particularly since these two heteroaromatic substrates have similar resonance hybrids (Figure 8B). However, the more electronegative oxygen compared to sulfur of **12** likely induced a larger δ^+ charge on the vicinal C_{ipso} of **7**. Moreover, the more electronegative oxygen of **7** distributes its lone pair electrons less than sulfur and thus likely reduced the magnitude of the negative charge (δ^-) in the canonical resonance structures at C_{ipso} (Figure 8B,

dx.doi.org/10.1021/cs500474s | ACS Catal. 2014, 4, 3077–3090

route b). A smaller magnitude negative charge (arbitrarily set at $0.5\delta^-$) at C_{ipso} was assigned for **7** along with a larger induced positive charge (assigned as "$0.75\delta^+$" due to the more electronegative O atom and adjacent δ^-) (see **25**), compared to the charges in **12** (see **24**). The relative magnitude of the δ^+ on C_{ipso} is deemed larger for **7** and thus was viewed to promote the removal of the H_β in the *Pa*PAM reaction. In addition, the higher proportion of (2-furyl)acrylate (65.2%) from **7** (compared to only 9.1% (2-thienyl)acrylate from **12**) suggests that the amination step during the conversion of **7** to β-**7** is negatively affected by its comparatively larger δ^+ on C_{ipso}.

Comparing the Effects of Regioisomeric Substituents on *Pa*PAM Catalysis and Substrate Affinity. The kinetic parameters of the *meta*/*para*/*ortho*-regioisomers (bromo-**2**/**15**/**20**; fluoro-**3**/**5**/**10**; chloro-**4**/**14**/**21**; nitro-**9**/**17**/**22**; methoxy-**11**/**18**/**19**; and methyl-**13**/**16**/**6**) were compared. The binding affinities (estimated by K_M) for the fluoro- and methyl-substrate trifecta were approximately of the same order. However, the K_M of *Pa*PAM for the *o*-methoxy substrate **19** was nearly 10-times smaller than for its *meta*- and *para*-isomers (Table 1). The K_I values (μM) for *o*-bromo- (**20**), *o*-chloro- (**21**), and *o*-nitro- (**21**) substrates were 25-times smaller than the K_M values of *Pa*PAM for the corresponding *meta*- and *para*-isomers. This supported the hypothesis that the *ortho*-substituted substrates generally bound *Pa*PAM better than the *meta*- and *para*-isomers.

The relative binding affinity of each substrate was assessed as a function of the six substituents (of varying electronic and steric effects) in the *ortho*-, *meta*-, or *para*-position. The relative binding affinities predicted from the calculated energies of protein−ligand interactions and the internal energy of the ligand $[E_{(p\text{-}l)} + E_{(l)}]$ in the absence of energy minimization matched the trend ($m \sim p > o$) in the experimental K_M values for substrate isomers with halogens or nitro substituents (Tables S1 and S2 of Supporting Information). This supports the predictive value of the model in which the binding site residues and substrate maintain the positions found in the crystal structure with α-phenylalanine. The calculated vdW interaction energies ($E_{V(p\text{-}l)}$) also follow the "$m \sim p > o$" trend, except for chloro compounds, which bound less tightly to *Pa*PAM (i.e., had higher K_M) than predicted by the $E_{V(p\text{-}l)}$ for chloro series compared to other halogenated substrates (Tables S1 and S2 of Supporting Information). The chloro series will be discussed further in the Activity Cliff Analysis section below.

Importantly, the binding affinity order for all substrates approximately corresponded to the vdW radii of the substituents. *Pa*PAM bound substrates with a fluoro group (~1.5 Å) the best, followed by methyl (~1.9 Å), then bromo and chloro groups (~1.8 Å). The least favorable substrate for binding to *Pa*PAM contained the bulkiest substituents: nitro (~3.1 Å vdW radius; estimated by the lengths of the C_{ar}−N plus the terminal N═O bond) and methoxy (~3.4 Å vdW radius; estimated by the lengths of the C_{ar}−O plus the methyl C−H bonds).[34,35] In general, *Pa*PAM was predicted by $E_{V(p\text{-}l)}$ to disfavor binding substrates with bulky groups at the *ortho*-position, which correlated well with the experimental K_M values. Surprisingly, substrates with *o*-methyl (**6**) (K_M = 88 μM) and *o*-methoxy (**19**) (K_M = 164 μM) groups bound *Pa*PAM better than expected from their calculated $E_{V(p\text{-}l)}$ (55 and 108 kcal/mol, respectively) (Tables S1 and S2 of Supporting Information). Binding of the *o*-methoxy group could become more energetically favorable if it rotated slightly from its crystallographic position to form hydrogen bonds with Tyr320 in *Pa*PAM (Figure S39 of Supporting Information).

Only three of the six *ortho*-isomers tested (fluoro, methoxy, and methyl) were productive. The k_{cat}^{total} of *Pa*PAM for the *m*-fluoro isomer (**3**, 0.031 s^{-1}) was only slightly greater than those for the *p*-fluoro (**5**, 0.023 s^{-1}) and *o*-fluoro (**10**, 0.022 s^{-1}) isomers (i.e., *meta*- $\gtrsim$ *para*- $\approx$ *ortho*-fluoro). The similar k_{cat} values among the fluoro regioisomers suggested that the rate of the *Pa*PAM-catalyzed isomerization is indifferent to the position of the fluoro group on the aryl ring. The turnover of the *m*-methoxy isomer (**11**, 0.203 s^{-1}) was 10-times faster than that for the *p*-methoxy isomer (**18**, 0.022 s^{-1}) and nearly 100-times faster than that for the *o*-methoxy substrate **19** (0.003 s^{-1}) (i.e., *meta*- $\gg$ *para*- > *ortho*-methoxy). As discussed previously, the *m*-methoxy of **11** is a "push−pull" substituent that releases and withdraws electron density with the aryl ring but is partially electron-withdrawing because of the electronegative oxygen atom. The balanced electronic effects were proposed to speed-up the hydroamination step (Figure 6C) yet not greatly retard the elimination step (Figure 6D). By contrast, the same substituent at the *para*- and *ortho*-positions places a δ^- charge directly on C_{ipso} connected to C_β and is therefore imagined to significantly slow the elimination step for the *para*/*ortho*-pair **18**/**19** (see Figure 6G or H).

The data show that *Pa*PAM generally catalyzed the *meta*- faster than the *para*- and *ortho*-substituted substrates containing electron-donating substituents. The only exception was the *o*-methyl regioisomer **6** (0.064 s^{-1}), which was turned over slightly better than the *m*-methyl isomer (**13**, 0.058 s^{-1}) and was ~4-fold better than the *p*-methyl isomer (**16**, 0.013 s^{-1}) (i.e., *ortho*- $\gtrsim$ *meta*- > *para*-methyl). It is unclear why the trend for the regioisomers of methylphenylalanine was an outlier among the other regioisomeric series. Perhaps some as yet unknown effect of the nonpolar *o*-methyl interacts with the *Pa*PAM active site better than the more polar *o*-methoxy- and *o*-fluoro-counterparts.

In addition, the k_{cat}^{total} values of *Pa*PAM for the *meta*-substrates of the *meta*/*para*-pairs (bromo-**2**/**15** and chloro-**4**/**14**) are about 10-times greater than those for the corresponding *p*-isomers. Similarly, the rate difference for the nitro-**9**/**17** *meta*/*para*-pair was approximately 4-fold, favoring the *meta*-substituted substrate (Table 1). As described earlier, the "push−pull" of the electron pairs and the electronegativity of chloro and bromo groups likely reduces their electron-withdrawing magnitude compared to that of the strongly electron-withdrawing nitro group. Thus, these electron-withdrawing substituents at the *meta*- or *para*-position place a δ^+ on C_{ipso} or inductively withdraw electron density from C_{ipso}, respectively. In general, this δ^+ charge distribution likely facilitates the elimination step (see Figure 6A and E) but likely impedes the hydroamination steps (see Figure 6B and F), with the nitro group doing so more strongly.

Product Distribution. The product pool catalyzed by *Pa*PAM for 11 of the 19 productive substrates comprised the aryl acrylate at <10% and the β-amino acid at >90%. As discussed earlier, *Pa*PAM converted **5** to an elevated proportion of *p*-fluorocinnamate (14.3%) over the amount of cinnamate byproduct made (at 7.2%) from the natural substrate **1**. Similarly, *Pa*PAM catalyzed a larger proportion of the cinnamate analogues from the *ortho*-isomers **6** (16.4% *o*-methylcinnamate) and **19** (30% *o*-methoxycinnamate), *para*-isomers **16** (36.4% *p*-methylcinnamate) and **17** (52.0% *p*-nitrocinnamate), *meta*-isomers **3** (14.8% *m*-fluorocinnamate)

dx.doi.org/10.1021/cs500474s | *ACS Catal.* 2014, 4, 3077−3090

and **13** (21.7% *m*-methylcinnamate), and the heteroaromatic compound **7** (65.2% (2-furyl)acrylate). As described earlier, we propose for these substrates that the amination rate was decreased by the electronic effects of the functional group.

Relationship between *Pa*PAM-Substrate Interaction Energies, Flexibility, and K_M. The calculated interaction energies obtained from modeling provided insight into which energy terms correlated best with the K_M values of *Pa*PAM for each substrate. They also helped elucidate which substrate-docking model correlated best with experimental K_M. The static model placed the substrates identical to the trajectory of α-phenylalanine in the crystal structure. The flexible model, however, allowed bond-rotational motion for the protein side chains to relieve unfavorable interactions. The static modeling showed that the experimental K_M for each substrate (except for three unreactive *o*-bromo, *o*-chloro, and *o*-nitro substrates **20**–**22**) increased with total energy $[E_{(p\text{-}l)} + E_{(l)}]$, which approximated $\Delta G_{binding}$ and reflected unfavorable interactions (Figure 10). The linear correlation coefficient (*ccoef*) between $[E_{(p\text{-}l)} + E_{(l)}]$ and K_M was 0.48 (Figure 10), while the *ccoef* between $E_{V(p\text{-}l)}$ and K_M was highest, at 0.54 (Figure S42 of the Supporting Information). Incidentally, the *ccoef* between the Coulombic energy $[E_{C(p\text{-}l)}]$, a component of $E_{(p\text{-}l)}$ and K_M, was lower (0.33; Figure S41 of the Supporting Information). These results suggested that the steric effects in the protein–ligand adduct and within the ligand are dominant over electrostatic interactions upon substrate binding. Moreover, when energy minimization was used to relieve vdW overlap between each substrate and the active site residues of *Pa*PAM (see Figure S42 of the Supporting Information), the *ccoef* between $[E_{(p\text{-}l)} + E_{(l)}]$ and K_M decreased from 0.48 to 0.35. This result emphasizes the importance of vdW overlap-induced strain in affecting the binding affinity of *Pa*PAM for its substrates.

Another reason why energy minimization of the protein–ligand interaction likely affected the correlation between $[E_{(p\text{-}l)} + E_{(l)}]$ and K_M is that, in some cases, groups were rotated that should have remained rigid. This may be due to inaccuracies in energy-minimization force field parameters for some functional groups, due to the prodigious challenge in deriving correct torsional energy barrier profiles for all bonds between all types of functional groups that occur in organic molecules. For instance, the nitro substituent was rotated out-of-plane relative to the phenyl ring during energy minimization. However, our analysis of 200 nitrophenyl groups in small-molecule crystal structures in the Cambridge Structural Database 1.1.1 (http://webcsd.ccdc.cam.ac.uk) indicated that 87.5% of the nitrophenyl groups are entirely coplanar, regardless of other features in the structure.[36] The energy minimization-free protocol provided intermolecular energy values that correlated better with K_M. This observation suggests that the crystallographic placement of the substrates and *Pa*PAM was ideal for most substrates and that modeling alternative, energy-minimized side group positions may reflect catalytically unproductive conformations.

Substrates were identified as either in the NH_2-*cis* or NH_2-*trans* configuration (Figure 9) if the difference (ΔE_{tot}) in the $[E_{(p\text{-}l)} + E_{(l)}]$ term for models of the two orientations was >25 kcal/mol (Table S3, Supporting Information). Using this limit, *o*-methoxy- (**19**), *m*-methyl (**13**), *m*-bromo- (**2**), *m*-nitro- (**9**), and *m*-chloro- (**4**) substrates were predicted to conform to the NH_2-*cis* configuration, while *p*-methoxy- (**18**), *o*-methyl- (**6**), *o*-chloro- (**21**), *o*-bromo- (**20**), and *o*-nitro- (**22**) substrates were predicted to favor the NH_2-*trans* configuration (Figure 10 and Table S3, Supporting Information). In substrate **18**, the methyl

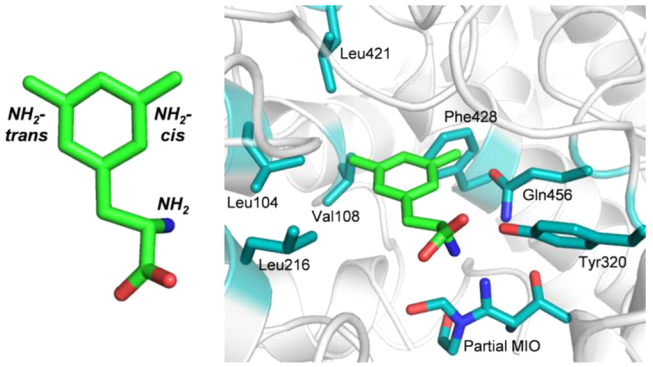

Figure 9. Overlay of the NH_2-*cis* and NH_2-*trans* configurations is illustrated, using the *m*-methyl-(*S*)-α-phenylalanine substrate (atoms are C, green; N, blue; and O, red). The methyl group can be positioned on the same side (NH_2-*cis*) or the opposite side (NH_2-*trans*) as the reactive amino group of the chiral substrate (left). An overlay of the NH_2-*cis* and NH_2-*trans* active configurations of *m*-methyl-(*S*)-α-phenylalanine is modeled in the crystallographic position of α-phenylalanine in *Pa*PAM (PDB ID 3UNV). A partial MIO and the active site residues that cause van der Waals overlap with the ligands are shown (C, light blue; N, dark blue; and O, red). SLIDE and other docking tools cannot model covalently bound ligands, which are interpreted as disallowed steric overlap (right). Thus, the alkene carbon atoms of the MIO (cf. Figure 2) were removed to dock the substrate.

of the methoxy group was predicted to adopt a quasi NH_2-*cis* configuration.

For *meta*-substituted substrates, the NH_2-*cis* is the preferred configuration because Leu104, Val108, and Leu421 sterically hinder the NH_2-*trans* conformers more than Gln456, Phe428, Gly85, Phe455, and Tyr320 hinder the NH_2-*cis* conformers (Figure 9). However, *m*-methoxy substrate **18** has no preference for the NH_2-*cis* or NH_2-*trans* configuration, as

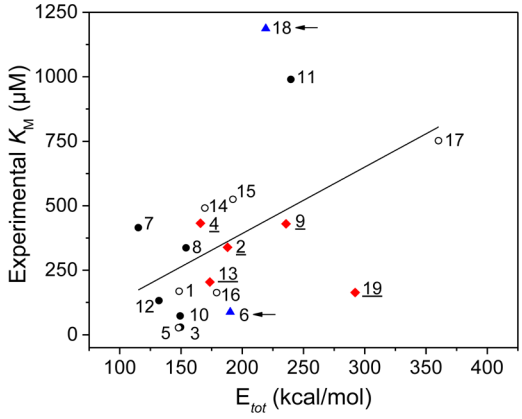

Figure 10. Plot of experimental K_M and $E_{tot} = E_{(p\text{-}l)}$ (protein–ligand interaction energy) + $E_{(l)}$ (the intraligand energy) calculated with Szybki. The substrates were modeled statically, according to the trajectory of α-phenylalanine in the *Pa*PAM crystal structure, without energy minimization. Substrates are labeled according to Table 1, and the lower energy of the two configurations [NH_2-*cis* (red ♦, underlined) and or NH_2-*trans* (blue ▲, with arrows)] is plotted for the substrates. Substrates with no significant difference in energy between the NH_2-*cis* and NH_2-*trans* (ΔE < 25 kcal/mol) are shown as filled circles (●). Substrates with *para*-substituents (except *p*-methoxy) without an NH_2-*cis* or NH_2-*trans* preference are shown as open-circles (○). Nonproductive substrates **20**–**22** (not shown) were predicted to prefer the NH_2-*trans* orientation in the *Pa*PAM active site.

dx.doi.org/10.1021/cs500474s | *ACS Catal.* 2014, 4, 3077–3090

energy calculations suggest that the methoxy group interacts similarly with active sites residues on either side. It should be noted that Phe428, Val108, and Leu421 also sterically hinder substrates with *para*-substituted substrates. The *ortho*-substituted substrates (except for the *o*-methoxy substrate **19**) are energetically more likely to adopt the NH_2-*trans* configuration. The *ortho*-substituted substrates have steric barriers created by residues Gln456, and Tyr320 on the NH_2-*cis* side of *Pa*PAM (Figure 9). In addition, the NH_2-*trans* conformers of the *ortho*-substituted substrates encounter lower $E_{V(p\text{-}l)}$ between Leu216 and Leu104 than between Tyr320 and Gln456 of the NH_2-*cis* conformers (Figure 9). As mentioned previously, the *o*-methoxy substrate **19** bound to *Pa*PAM better than expected from its calculated vdW energy ($E_{V(p\text{-}l)}$) (Tables S1 and S2, Supporting Information). The energy calculations predict that **19** favors the NH_2-*cis* conformer. This orientation is consistent with the hypothesis that the *o*-methoxy of **19** is near Tyr320 of *Pa*PAM and can potentially form an energetically favorable hydrogen bond (Figure S39 of Supporting Information). Of the nine substrates (**1**, **3**, **5**, **6**, **10**, **12**, **13**, **16**, and **19**) that bound *Pa*PAM the best ($K_M \lesssim 200$ μM, i.e., not >20% over the K_M of *Pa*PAM for **1**), all except the *o*-methoxy substrate **19** ($E_{V(p\text{-}l)}$ = 108 kcal/mol) had $E_{V(p\text{-}l)} \leq 55$ kcal/mol (designated as the energy threshold with low vdW overlap). However, the majority of the poorest binding substrates, with $K_M > 500$ μM, and nonproductive substrates had $E_{V(p\text{-}l)} \geq 80$ kcal/mol, with the *p*-nitro- (**17**), *o*-bromo- (**20**), and *o*-nitro- (**22**) substrates predicted to have comparatively higher vdW energy at ≳190 kcal/mol (Table S3, Supporting Information). Relative binding energy, based on $E_{V(p\text{-}l)}$, is thus highly predictive of *Pa*PAM having a potentially high or low affinity for a substrate.

Generally, for productive substrates where the K_M of *Pa*PAM was ≤500 μM, the relative energy $[E_{(p\text{-}l)} + E_{(l)}]$ of the NH_2-*cis* and NH_2-*trans* configurations tended to be ≤200 kcal/mol (see Table S3, Supporting Information). It was intriguing to find that substrates that bind *Pa*PAM with the least affinity (highest K_M) (compound **18**) or were nonproductive (**21**, **20**, and **22**) had differences of ≳150 kcal/mol between the two orientations (see Table S3, Supporting Information). These results suggest that either the substituent on the substrate causes the enzyme to preferentially bind the substrate in one orientation over the other or that low vdW barriers in the pocket enable the substrate to rotate to an active conformation for turnover.

The computational analyses identified residues that will help guide future mutational studies. Proposed mutations are envisioned to increase the binding affinity of *Pa*PAM for various substrates. The K_M of *Pa*PAM was higher for several substrates with *meta*- and *para*-substituents (except fluoro and methyl) than for **1**. The presumed lower binding affinity was likely due to steric interactions between the substituents and the active site residues of *Pa*PAM. As mentioned herein, *meta*-substituted substrates were shown by modeling to prefer the NH_2-*cis* configuration to avoid steric clashes with branched hydrophobic residues. Mutation of Leu104, Val108, and Leu421 to alanines may improve the binding of *meta*-substituted substrates by providing flexibility to bind in the NH_2-*cis* or NH_2-*trans* configuration. Further, computational models predicted that *para*-substituents sterically clash with Phe428, Val108, and Leu421. Therefore, exchange of these residues for alanine may facilitate the binding of *para*-substituted substrates. Surprisingly, the computational analysis predicted that all *ortho*-substituted α-arylalanines bound well to *Pa*PAM; however, relief of the active site sterics may enable these *ortho*-substituted α-arylalanines to better access a catalytically competent conformation and improve the turnover number for these substrates. Some of the computationally predicted targets for mutation are supported, in part, by an earlier study on a related, MIO-dependent phenylalanine ammonia lyase. The earlier work showed that a Val83Ala mutation (positioned analogously to Val108 of *Pa*PAM) in the substrate binding pocket resulted in enzyme catalytic efficiency at ∼4-fold greater than that of the wild-type enzyme. The efficiency enhancement of the mutant resulted from a ∼5-fold reduction in K_M and a ∼20-fold increase in k_{cat} compared to the parameters of the wild-type enzyme.[37]

The flexible docking feature of SLIDE provided another approach to reduce vdW collisions between the crystallographic conformation of *Pa*PAM side chains and substituents on the arylalanine substrates oriented in the NH_2-*cis* and NH_2-*trans* configurations. After application of the SLIDE flexibility modeling in the site, no significant correlation was found for SLIDE-calculated interaction energies and K_M values except for the unsatisfied polar interaction term: $E_{(p\text{-}l)}$ (*ccoef* = 0.13), hydrophobic interaction energy, $E_{H(p\text{-}l)}$ (*ccoef* = −0.19), and unfavorable energy of interaction due to unpaired or repulsive polar interactions, $E_{UP(p\text{-}l)}$ (*ccoef* = 0.44). SLIDE also assessed the sum of unresolvable vdW overlaps in each complex, in Å, following flexibility modeling. The correlation of this value with K_M, *ccoef* = 0.27, was positive but somewhat lower than the correlation found between the Szybki intermolecular vdW energy and K_M in the absence of substrate or protein motion relative to the crystal structure (*ccoef* of 0.54). This is consistent with the decrease in correlation between Szybki intermolecular vdW energy and K_M (from 0.54 to 0.42) upon energy minimization, reflecting changes in the conformation of the complex. These results indicate that the favorability of vdW interactions and the absence of unsatisfied polar interactions when the substrate and protein are in their crystallographic conformation are the strongest predictors for favorable substrate K_M.

Activity Cliff Analysis. SALI values were used to identify "activity cliffs" that represent large changes in *Pa*PAM binding affinity among structurally similar substrates.[22] The most obvious activity cliffs were found for substrates with fluoro-, methyl-, and chloro-substituents at the same positions (Figure 11). The chloro- and methyl-groups share similar vdW radii. When chloro is attached to an aryl ring carbon, its electron density delocalizes through resonance, placing a partial positive charge at the pole of the chloro atom furthest from the ring carbon.[38] The polarizability of the halogen atoms increases with atomic orbital size; therefore, the trend to form a halogen bond is in the order fluoro < chloro < bromo < iodo, where iodo normally forms the strongest interactions. Thus, the chloro- and bromo-substituents of substrates used in this study can act as electrophiles and might potentially form halogen bonds with nearby electron donor atoms, such as oxygen.

Favorable halogen-bonds between the halogen acceptor (X) and donor (O) have a C−X···O angle of ∼165° or a C−O···X angle of ∼120°, with a distance between X and O of ∼3 Å.[38] However, the structure calculations and modeling revealed no evidence for chloro- or bromo-bonding between *Pa*PAM and the active orientation of the *o*-, *m*-, or *p*-chloro- or -bromo-substrates, based on searching for appropriate halogen-bond donors within 4 Å of the halogen. It is worth noting that the incompatibility between charged chloro groups and surrounding neutral carbon atoms in the binding pocket of *Pa*PAM may

dx.doi.org/10.1021/cs500474s | *ACS Catal.* 2014, 4, 3077−3090

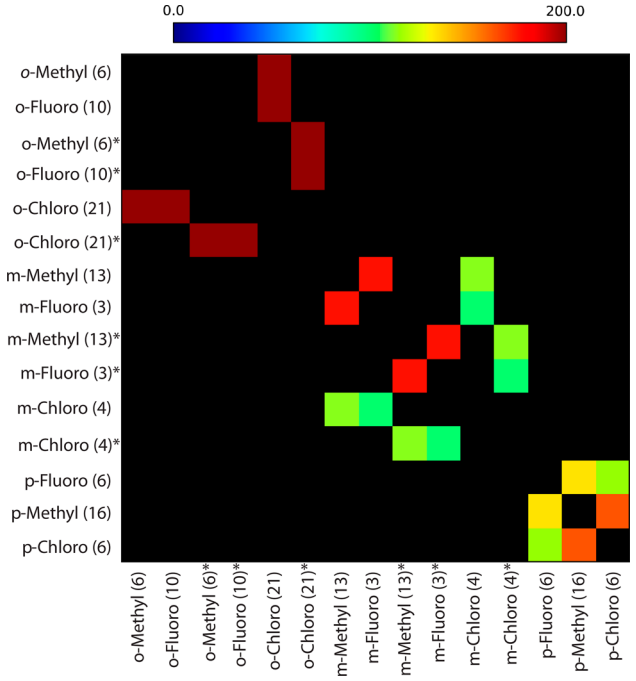

Figure 11. Structure−activity landscape index (SALI) analysis showing the subset of substrate pairs exhibiting a large change in K_M value upon a small change in structure. Substrate pairs with SALI scores near 200 (approaching red) indicate the most significant activity cliffs. Asterisks (*) indicate substrates in NH_2-*cis* configuration; all others are NH_2-*trans*.

contribute to the higher K_M values for compounds with chloro-substituents relative to those with isosteric methyl-substituents. The *o*-, *m*-, and *p*-fluoro substrates bound *Pa*PAM (K_M values between 27 and 73 μM) better than natural substrate **1** (K_M = 168 μM), indicating a more favorable interaction between the fluoro group and surrounding hydrocarbon side chains.

CONCLUSIONS

In summary, vdW overlaps, estimated by the $E_{V(p\text{-}l)}$ in Szybki, and the total sum (in Å) of vdW overlaps remaining following SLIDE docking, are most significant between the substrates and residues Phe428, Val108, Leu421, Leu104, Gln456, and Tyr320 of *Pa*PAM (Figure 9), which largely influence binding affinity. Substrates without substituents on the aryl rings, the natural substrate **1**, 2-furyl- (**7**), 2-thienyl- (**24**) and 3-thienyl- (**8**) alanine have no steric collisions with the binding site residues. This substrate specificity study was not exhaustive; there remain several arylalanine analogues to be tested in *Pa*PAM kinetics studies.

In the present study, the dependence of the reaction rate on *Pa*PAM-catalyzed α/β-isomerization was probed with several arylalanine analogues. The influence of the substituents on the k_{cat} of *Pa*PAM revealed a concave-down or a downward break in correlations with Hammett substituent constants (σ). The trend of these correlations[31] suggests that the rate-determining step changes from the elimination step to the hydroamination step according to the direction and magnitude of the electronic properties of the substituent. In addition, the computational analyses provided a means by which to predict the docking conformation of 22 substituted arylalanine substrates. This information will guide future targeted amino acid mutagenesis of *Pa*PAM to increase the catalytic efficiency by improving the binding affinity for various other non-natural substrates.

ASSOCIATED CONTENT

Supporting Information

Gas chromatography and mass spectrometry, enzyme kinetics, and computational energy data. This material is available free of charge via the Internet at http://pubs.acs.org.

AUTHOR INFORMATION

Corresponding Authors

*(L.A.K.) E-mail: KuhnL@msu.edu.
*(K.D.W.) E-mail: walke284@msu.edu.

Author Contributions

‖N.D.R. and N.L. contributed equally to this work.

Notes

The authors declare no competing financial interest.

ACKNOWLEDGMENTS

We thank OpenEye Scientific Software for academic licensing of QUACPAC, OMEGA, Szybki, and ROCS software. This material is based on work supported by NSF-CAREER Award 0746432 and Michigan State University AgBioResearch RA078692 (894).

REFERENCES

(1) Horne, W. S. *Expert Opin. Drug Discovery* **2011**, *6*, 1247−1262.
(2) Ruf, S.; Buning, C.; Schreuder, H.; Horstick, G.; Linz, W.; Olpp, T.; Pernerstorfer, J.; Hiss, K.; Kroll, K.; Kannt, A.; Kohlmann, M.; Linz, D.; Hübschle, T.; Rütten, H.; Wirth, K.; Schmidt, T.; Sadowski, T. *J. Med. Chem.* **2012**, *55*, 7636−7649.
(3) Huang, X.; O'Brien, E.; Thai, F.; Cooper, G. *Org. Process Res. Dev.* **2010**, *14*, 592−599.
(4) Jennewein, S.; Wildung, M. R.; Chau, M. D.; Walker, K.; Croteau, R. *Proc. Natl. Acad. Sci. U.S.A.* **2004**, *101*, 9149−9154.
(5) Klettke, K. L.; Sanyal, S.; Mutatu, W.; Walker, K. D. *J. Am. Chem. Soc.* **2007**, *129*, 6988−6989.
(6) Magarvey, N. A.; Fortin, P. D.; Thomas, P. M.; Kelleher, N. L.; Walsh, C. T. *ACS Chem. Biol.* **2008**, *3*, 542−554.
(7) Chesters, C.; Wilding, M.; Goodall, M.; Micklefield, J. *Angew. Chem., Int. Ed.* **2012**, *51*, 4344−4348.
(8) Feng, L.; Wanninayake, U.; Strom, S.; Geiger, J.; Walker, K. D. *Biochemistry* **2011**, *50*, 2919−2930.
(9) Röther, D.; Poppe, L.; Morlock, G.; Viergutz, S.; Rétey, J. *Eur. J. Biochem.* **2002**, *269*, 3065−3075.
(10) Krug, D.; Mueller, R. *ChemBioChem* **2009**, *10*, 741−750.
(11) Christenson, S. D.; Liu, W.; Toney, M. D.; Shen, B. *J. Am. Chem. Soc.* **2003**, *125*, 6062−6063.
(12) Huang, S. X.; Lohman, J. R.; Huang, T.; Shen, B. *Proc. Natl. Acad. Sci. U.S.A.* **2013**, *110*, 8069−8074.
(13) Strom, S.; Wanninayake, U.; Ratnayake, N. D.; Walker, K. D.; Geiger, J. H. *Angew. Chem., Int. Ed.* **2012**, *51*, 2898−2902.
(14) Hawkins, P. C.; Skillman, A. G.; Warren, G. L.; Ellingson, B. A.; Stahl, M. T. *J. Chem. Inf. Model.* **2010**, *50*, 572−584.
(15) Hawkins, P. C.; Nicholls, A. *J. Chem. Inf. Model.* **2012**, *52*, 2919−2936.
(16) Jakalian, A.; Jack, D. B.; Bayly, C. I. *J. Comput. Chem.* **2002**, *23*, 1623−1641.
(17) Nicholls, A.; Wlodek, S.; Grant, J. A. *J. Comput.-Aided Mol. Des.* **2010**, *24*, 293−306.
(18) Wlodek, S.; Skillman, A. G.; Nicholls, A. *J. Chem. Theory Comput.* **2010**, *6*, 2140−2152.
(19) Halgren, T. A. *J. Comput. Chem.* **1996**, *17*, 490−519.
(20) Zavodszky, M. I.; Rohatgi, A.; Van Voorst, J. R.; Yan, H.; Kuhn, L. A. *J. Mol. Recognit.* **2009**, *22*, 280−292.

(21) Zavodszky, M. I.; Sanschagrin, P. C.; Korde, R. S.; Kuhn, L. A. *J. Comput.-Aided Mol. Des.* **2002**, *16*, 883−902.
(22) Guha, R.; Van Drie, J. H. *J. Chem. Inf. Model.* **2008**, *48*, 646−658.
(23) Hawkins, P. C.; Skillman, A. G.; Nicholls, A. *J. Med. Chem.* **2007**, *50*, 74−82.
(24) Mutatu, W.; Klettke, K. L.; Foster, C.; Walker, K. D. *Biochemistry* **2007**, *46*, 9785−9794.
(25) Schuster, B.; Rétey, J. *Proc. Natl. Acad. Sci. U.S.A.* **1995**, *92*, 8433−8437.
(26) Wanninayake, U.; DePorre, Y.; Ondari, M.; Walker, K. D. *Biochemistry* **2011**, *50*, 10082−10090.
(27) Weiner, B.; Szymanski, W.; Janssen, D. B.; Minnaard, A. J.; Feringa, B. L. *Chem. Soc. Rev.* **2010**, *39*, 1656−1691.
(28) Szymanski, W.; Wu, B.; Weiner, B.; de Wildeman, S.; Feringa, B. L.; Janssen, D. B. *J. Org. Chem.* **2009**, *74*, 9152−9157.
(29) Ratnayake, N. D.; Wanninayake, U.; Geiger, J. H.; Walker, K. D. *J. Am. Chem. Soc.* **2011**, *133*, 8531−8533.
(30) Hammett, L. P. *J. Am. Chem. Soc.* **1937**, *59*, 96−103.
(31) Hoffmann, J.; Klicnar, J.; Štěrba, V.; Večeřa, M. *Collect. Czech. Chem. Commun.* **1970**, *35*, 1387−1398.
(32) Fernández, I.; Wu, J. I.; von Ragué Schleyer, P. *Org. Lett.* **2013**, *15*, 2990−2993.
(33) Laing, M. *J. Chem. Educ.* **1987**, *64*, 124.
(34) Batsanov, S. S. *Russ. Chem. Bull.* **1995**, *44*, 18−23.
(35) Li, A. J.; Nussinov, R. *Proteins* **1998**, *32*, 111−127.
(36) Carpy, A. J. M.; Haasbroek, P. P.; Ouhabi, J.; Oliver, D. W. *J. Mol. Struct.* **2000**, *520*, 191−198.
(37) Xiang, L.; Moore, B. S. *J. Bacteriol.* **2005**, *187*, 4286−4289.
(38) Metrangolo, P.; Meyer, F.; Pilati, T.; Resnati, G.; Terraneo, G. *Angew. Chem., Int. Ed.* **2008**, *47*, 6114−6127.